






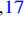







Publication Year	2018
Acceptance in OA @INAF	2020-10-13T16:06:38Z
Title	Improved 21 cm Epoch of Reionization Power Spectrum Measurements with a Hybrid Foreground Subtraction and Avoidance Technique
Authors	Kerrigan, Joshua R.; Pober, Jonathan C.; Ali, Zaki S.; Cheng, Carina; Beardsley, Adam P.; et al.
DOI	10.3847/1538-4357/aad8bb
Handle	http://hdl.handle.net/20.500.12386/27782
Journal	THE ASTROPHYSICAL JOURNAL
Number	864



Improved 21 cm Epoch of Reionization Power Spectrum Measurements with a Hybrid Foreground Subtraction and Avoidance Technique

Joshua R. Kerrigan¹ , Jonathan C. Pober¹ , Zaki S. Ali², Carina Cheng², Adam P. Beardsley³ , Aaron R. Parsons^{2,4}, James E. Aguirre⁵ , Nichole Barry⁶, Richard F. Bradley^{7,8,9}, Gianni Bernardi^{10,11,12} , Chris L. Carilli^{13,14} , David R. DeBoer⁴ , Joshua S. Dillon^{2,4,15,17} , Daniel C. Jacobs³ , Saul A. Kohn⁵ , Matthew Kolopanis^{3,16}, Adam Lanman¹, Wenyang Li¹, Adrian Liu^{2,15,18} , and Ian Sullivan⁶

¹ Department of Physics, Brown University, Providence RI, USA; joshua_kerrigan@brown.edu

² Department of Astronomy, University of California, Berkeley CA, USA

³ School of Earth and Space Exploration, Arizona State University, Tempe AZ, USA

⁴ Radio Astronomy Lab., University of California, Berkeley CA, USA

⁵ Department of Physics and Astronomy, University of Pennsylvania, Philadelphia PA, USA

⁶ Department of Physics, University of Washington, Seattle WA, USA

⁷ Department of Electrical and Computer Engineering, University of Virginia, Charlottesville VA, USA

⁸ National Radio Astronomy Observatory, Charlottesville VA, USA

⁹ Department of Astronomy, University of Virginia, Charlottesville VA, USA

¹⁰ INAF—Istituto di Radioastronomia, Italy

¹¹ Square Kilometer Array, South Africa, Cape Town South Africa

¹² Department of Physics and Electronics, Rhodes University, South Africa

¹³ National Radio Astronomy Observatory, Socorro NM, USA

¹⁴ Astrophysics Group, Cavendish Lab., Cambridge UK, USA

¹⁵ Berkeley Center for Cosmological Physics, Berkeley CA, USA

¹⁶ Department of Physics, Arizona State University, Tempe AZ, USA

Received 2017 December 21; revised 2018 June 8; accepted 2018 August 5; published 2018 September 10

Abstract

Observations of the 21 cm Epoch of Reionization signal are dominated by Galactic and extragalactic foregrounds. The need for foreground removal has led to the development of two main techniques, often referred to as “foreground avoidance” and “foreground subtraction.” Avoidance is associated with filtering foregrounds in Fourier space, while subtraction uses an explicit foreground model that is removed. Using 1088 hr of data from the 64-element PAPER array, we demonstrate that subtraction of a foreground model prior to delay-space foreground filtering results in a modest but measurable improvement of the performance of the filter. This proof-of-concept result shows that improvement stems from the reduced dynamic range requirements needed for the foreground filter: subtraction of a foreground model reduces the total foreground power, so for a fixed dynamic range, the filter can push toward fainter limits. We also find that the choice of window function used in the foreground filter can have an appreciable affect on the performance near the edges of the observing band. We demonstrate these effects using a smaller 3 hr sampling of data from the MWA, and find that the hybrid filtering and subtraction removal approach provides similar improvements across the band as seen in the case with PAPER-64.

Key words: dark ages, reionization, first stars – methods: data analysis – techniques: interferometric

1. Introduction

The 21 cm Epoch of Reionization (EoR) signal is faint emission produced from neutral hydrogen in the period directly following the formation of the first stars and galaxies. We can attempt to observe this redshift-evolving signal using radio interferometer arrays with a wide instantaneous bandwidth. Unfortunately, we are limited by what we can observe due in part to Galactic and extragalactic foregrounds concealing the 21 cm signal in our observations. First-generation 21 cm interferometers such as the Murchison Widefield Array (MWA) (Tingay et al. 2013), the Donald C. Backer Precision Array for Probing the Epoch of Reionization (PAPER) (Parsons et al. 2010), and the LOw Frequency Array (LOFAR) (van Haarlem et al. 2013) have each developed independent techniques for addressing these foregrounds in their observations. The MWA and LOFAR have developed algorithms to fit and subtract accurate foreground models to observations, while PAPER uses foreground “avoidance” by filtering in Fourier

space on individual visibilities per baseline and per time. There is, however, no a priori reason that these techniques can only be applied to their respective telescopes.

Practically speaking, there are potential limitations. For example, PAPER uses redundant array configurations, and so its ability to accurately model foregrounds is limited by the point-spread function (PSF) and (u, v) coverage of the array. Similarly, the MWA has more complicated structure in its frequency response due to the polyphase filter bank (Offringa et al. 2016) and cable reflections (Ewall-Wice et al. 2016). This may require a wider delay-space filter in the MWA case to remove significant foreground power.

In this work, we present a method using both model-based foreground subtraction and delay-space filtering. Applied to both data from PAPER and the MWA, we find improvements in 21 cm EoR power spectrum sensitivities over all redshifts. In Section 2 we provide the motivation for removing foregrounds in our observations and the need for additional foreground suppression. Section 3 introduces the delay spectrum and filtering technique as applied in past PAPER analyses and describes how it is used in this work. Section 4 describes how the foreground models to be

¹⁷ NSF Astronomy and Astrophysics Postdoctoral Fellow.

¹⁸ Hubble Fellow.

subtracted are processed and applied to PAPER visibilities. In Section 5 we provide specifications for the PAPER and MWA data used for this analysis. In Section 6 we compare the result of our hybrid technique with both the PAPER power spectrum pipeline as presented in Ali et al. (2015) and a technique using only model-based foreground subtraction. Our technique is additionally applied to MWA observations, the results of which are described in Section 7. Finally, in Section 8, we conclude by discussing the implications of using foreground filtering and subtraction for future power spectra analyses.

2. Background

Galactic and extragalactic foregrounds dominate the cosmological signal in 21 cm EoR experiments, and must be removed if a detection of the 21 cm signal is to be achieved. Several foreground mitigation techniques have been applied independently to arrays such as PAPER, MWA, and LOFAR (see e.g., Liu & Tegmark 2011; Parsons et al. 2012, 2014; Vedantham et al. 2012a; Dillon et al. 2013, 2015; Wang et al. 2013; Liu et al. 2014a, 2014b; Pober et al. 2016; Trott et al. 2016). Some novel examples include a non-parametric generalized morphological component analysis (GMCA) wavelet decomposition (Chapman et al. 2013) used by LOFAR (Patil et al. 2017) and a singular-value decomposition (SVD) technique that is shown to isolate smooth spectrum foregrounds in GMRT visibilities while making no a priori assumptions about their form (Paciga et al. 2013).

Our point of reference begins with the foreground filtering technique used in Ali et al. (2015) on PAPER-64 observations. This filtering technique uses a wide-band iterative deconvolution filtering approach for removing bright foregrounds, which we describe in more detail in Section 3. This filtering, however, comes at the cost of losing all EoR information at the lowest Fourier modes where foregrounds reside.¹⁹ Foreground subtraction is a method employed by both the MWA and LOFAR (Beardsley et al. 2016; Jacobs et al. 2016; Patil et al. 2017), where one simulates visibilities corresponding to an accurate foreground model and subtracts them from the data. Unlike filtering, this method should ideally retain EoR information at all Fourier modes.

The motivation behind integrating these two techniques into a single power spectrum pipeline is to further reduce band-limited spectral leakage²⁰ of foreground power into high cosmological line-of-sight Fourier modes, k_{\parallel} , beyond what is capable with a filter alone (Morales et al. 2012; Parsons et al. 2012; Vedantham et al. 2012b; Pober et al. 2013). Analogously with a time series of finite data, a windowing function can be applied to reduce spectral leakage. This provides a reasonable way to mitigate any power seeping into neighboring bins in frequency space when taking the Fourier transform, but it comes at the expense of reduced sensitivity and correlated measurements. Subtracting a foreground model can reduce the dynamic range required in the frequency Fourier transform to k_{\parallel} , mitigating the need for more aggressive windowing functions (e.g., a Blackman-Harris convolved with itself, as in Thyagarajan et al. 2016).

¹⁹ This filtering technique is widely associated with the terminology of “foreground avoidance.” The goal is to keep high- k_{\parallel} modes (the so-called “EoR window”) of the 21 cm power spectrum clear of foreground contamination, at the cost of indiscriminately removing power from low- k_{\parallel} modes. Hence, these low- k , foreground contaminated modes are “avoided.”

²⁰ Commonly in digital signal processing, spectral leakage is associated with power contaminating neighboring bins in frequency when Fourier transforming from a time series to a frequency spectrum. In the work outlined here we refer to spectral leakage as contamination in nearby delay (τ) bins when transforming from a frequency space.

3. Wide-band Delay Filtering for Foreground Avoidance

To understand the wide-band delay filtering method employed in PAPER we begin with an explanation of the delay spectrum approach. We use the alternative form of the standard radio interferometer visibility equation

$$\begin{aligned} V_b(\nu) &= \int dl dm A(\nu, l, m) I(\nu, l, m) e^{-2\pi i(u l + v m)} \\ &= \int dl dm A(\nu, l, m) I(\nu, l, m) e^{-2\pi i v \tau_g} \end{aligned} \quad (1)$$

where $V_b(\nu)$ is the visibility of baseline b at observing frequency ν , $A(\nu, l, m)$ is the antenna response, $I(\nu, l, m)$ is the specific intensity distribution on the sky, (l, m) are the direction cosines on the sky, and (u, v) are the projected lengths of the baseline in units of wavelength. This form of the interferometer visibility equation is especially useful for demonstrating the delay spectrum approach because we can associate sources on the sky with a geometric delay, τ_g . This geometric delay

$$\tau_g = \frac{\mathbf{b} \cdot \hat{s}}{c} = \frac{1}{c}(b_x l + b_y m) \quad (2)$$

corresponds to the light travel time distance between two antennas for an emission from the direction \hat{s} , and directly relates to the baseline lengths $\mathbf{b} = (b_x, b_y)$ and the visibility domain coordinates with $\mathbf{u} = \nu \mathbf{b}/c$. By then applying a window function $W(\nu)$, and taking the Fourier transform over frequency of Equation (1),

$$\begin{aligned} \tilde{V}_b(\tau) &= \int_{-\infty}^{\infty} d\nu W(\nu) V_b(\nu) e^{-2\pi i \nu \tau} \\ &= \int_{-\infty}^{\infty} d\nu W(\nu) \left[\int dl dm A(\nu, l, m) \right. \\ &\quad \times I(\nu, l, m) e^{-2\pi i v \tau_g} \left. \right] e^{2\pi i v \tau} \\ &= \int dl dm [\tilde{W}(\tau) * \tilde{A}(\tau, l, m) * \tilde{I} \\ &\quad \times (\tau, l, m) * \delta(\tau - \tau_g)] \end{aligned} \quad (3)$$

we have what is called the delay transform, as found in Parsons & Backer (2009). This means that point sources on the sky can be mapped from our visibility to a geometric delay in delay space. Flat spectrum sources are constrained to a maximum geometric delay, τ_h , the horizon limit.²¹ This maximum delay is achieved when the direction from the baseline to the source on the sky, \hat{s} , is parallel to the baseline \mathbf{b} , which means the source is located at the horizon. When measuring the relatively weak 21 cm EoR signal, spectral leakage when taking the delay transform is significant. The foreground-dominated delays at $|\tau| \leq |\tau_H|$ can be approximately 10^5 larger in amplitude than the EoR modes being contaminated at $|\tau| > |\tau_H|$.

We also want to be able to associate our geometric delays with cosmological scales, which we can do using

$$\begin{aligned} k &= \sqrt{k_{\parallel}^2 + k_{\perp}^2} \\ &\approx \frac{2\pi H(z)}{\lambda(1+z)} |\tau| \end{aligned} \quad (4)$$

²¹ The intrinsic spectrum of the source expands its footprint in delay space beyond that of a delta function, but smooth spectrum sources (like foregrounds) will still have compact footprints and limited extent beyond the baseline’s delay horizon, τ_h , which is a direct consequence from Equation (3).

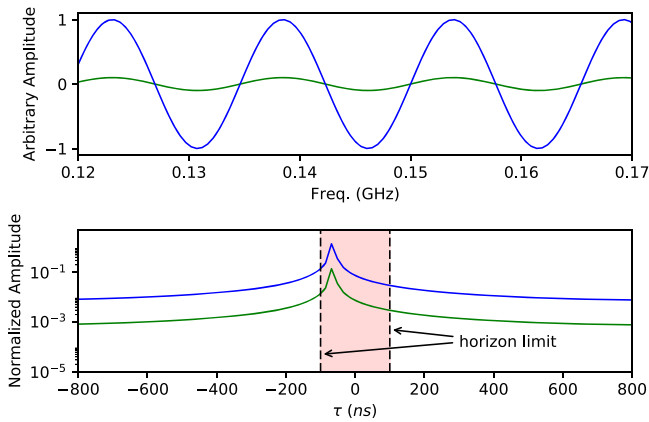


Figure 1. Toy model example of a single source near the horizon as it appears in a baseline visibility amplitude (top) and its delay transform (bottom), demonstrating how it appears near the horizon limit. The green line represents a 60% partial removal of the blue point source. Even the partial subtraction of a source can produce a non-negligible reduction in spectral leakage to delay bins outside of the horizon limit.

which directly relates the cosmological line of sight k_{\parallel} and its perpendicular k_{\perp} , where λ is the band center wavelength, z is the redshift of the observation, c is the speed of light, and $H(z)$ is the Hubble parameter. For our case of moving between delays and k space for PAPER-64 we can approximate $k_{\perp} \approx 0$ because of the short baselines involved; this is not true for our MWA analysis which spans baselines comparable to and much longer than PAPER-64.

A toy model demonstrating an example of spectral leakage can be seen in Figure 1, where a single point source spectrum near the horizon is shown in visibility space (top) at full intensity (blue) and reduced by 60% (green). The delay spectrum (bottom) shows the full and reduced intensity point source. Both have sidelobes that contaminate higher delays, but the reduced source has a proportionally reduced spectral leakage in delay space. Thus, even a partial foreground subtraction can free up more sensitivity to k -modes where we are more likely to make a statistical EoR detection.

The approximation of foreground sources being confined within a maximum delay, τ_h , gives us a natural motivation to filter out low delays. This filtering removes the foregrounds that occupy low delay modes, and in turn will reduce spectral leakage of foreground power into modes beyond τ_h . However, due to discontinuities in the visibility sampling function (e.g., missing data from radio frequency interference (RFI) and a finite band i.e., convolution with a top-hat window function), foreground power is scattered to high delays and thus a simple delay-space filter is insufficient for mitigating spectral leakage (Parsons & Backer 2009; Parsons et al. 2012, 2014). The delay filtering in the PAPER-64 power spectrum pipeline uses the application of a per baseline and per time wide-band deconvolution filter that iteratively fits components in delay space to remove foregrounds. We describe how the wide-band delay filter is implemented here in a succinct manner so as to motivate our foreground subtraction approach for mitigating any spectral leakage from this process. A more in-depth explanation of the filtering approach is outlined in Parsons et al. (2012).

The deconvolution process works in delay space. Since the sampling function in frequency is known, one can calculate the delay-space convolving kernel created by the sampling. The algorithm then simply finds the brightest delay mode and subtracts a fraction of its power, accounting for the convolving kernel that

correlates it with all other delay modes.²² The range of modes that are fit in delay space can be restricted to be within the horizon limit (or, typically, a small buffer of 15 ns beyond the horizon limit) so that no signal is removed from the higher delays. This process is iterated until a predetermined foreground residual threshold is met. This threshold is determined by the ratio of the initial to the final amplitude, which for the purpose of demonstrating this technique we take as 10^{-9} . We choose 10^{-9} because it provides the minimum amount of worst-case signal loss (<5% signal loss) at the modes nearest the horizon (Ali et al. 2015) and deconvolves the maximum amount of the sampling function while still converging. Decreasing the order of this threshold or using a more sparse sampling/windowing function can lead to the algorithm’s inability to converge, giving results with reduced filtering. We provide additional statistics in Appendix A for understanding how both a Blackman–Harris or top-hat window function with various thresholds affect the signal loss when applying the iterative wide-band deconvolution filter.

4. Foreground Subtraction Methodology

Foreground subtraction is achieved by forward modeling a source catalog to match observations. This model can come from an external catalog, or can be created from the data themselves, typically through a source-finding algorithm in image space. Because of its limited imaging capabilities and poor PSF, we do not want to use data from PAPER to create a foreground model. Rather, we use the GaLactic and Extragalactic All-sky Murchison Widefield Array (GLEAM; Hurley-Walker et al. 2017), described in Section 4.1. To generate and subtract model visibilities, we use the Fast Holographic Deconvolution (FHD; Sullivan et al. 2012) software package. The specifics of the visibilities generated for this work are described in Section 4.2.

4.1. Model Catalog

The standard MWA GLEAM catalog contains approximately 300,000 point sources across 30,000 deg². For this work, we use a modified GLEAM catalog which includes Pictor A²³ and Fornax A, both of which are treated as point sources given PAPER’s resolution.

It should also be noted that the catalog contains an observing gap from 6^h30^m to 7^h30^m local sidereal time (LST) to avoid the Galactic plane, which lies at the tail end of the available PAPER-64 observational data. We choose to focus on the LST range (1–6 hr) where known sources were subtracted and thus ignore the observational data where gaps in the GLEAM catalog exist. PAPER also has a non-trivial response to bright sources above the maximum GLEAM declination of +30° (e.g., Cygnus A). These sources have not been modeled or removed from the data.

²² In previous publications, this filtering has been referred to as CLEAN or a variant thereof, leading to some confusion. This iterative deconvolution process is based on the CLEAN algorithm as outlined in Högbom (1974), but there are no imaging or other steps associated with typical radio astronomy CLEAN algorithms. The PAPER wide-band delay filtering is similar only in the iterative process of deconvolving the maximal point in 1D delay space.

²³ We use a value of Pictor A’s flux density which is 10% higher than that from Jacobs et al. (2013). This factor is an approximate correction for the flux density scaling issues between the VLSS survey (Cohen et al. 2007) and the VLSSR survey (Lane et al. 2014) used as part of the Markov chain Monte Carlo pipeline of Jacobs et al. (2013).

4.2. Model Visibility Parameters

FHD has three primary functions: Simulation, Deconvolution, and Firstpass. The Deconvolution feature allows for full deconvolution of sources using a modified CLEAN algorithm (Högbom 1974; Sullivan et al. 2012). Using FHD’s full deconvolution is both time consuming and computationally expensive, and thus is not reasonable to fully deconvolve foregrounds from a 128 day data set. We choose to use the Firstpass feature, which accepts a source catalog, a primary beam model (Pober et al. 2012), and the antenna layout which is then forward modeled to match a given observation. This reduces the time for modeling (approximately 10,000 point sources) and subtraction of a single 10 min PAPER-64 observation to ~ 20 min using considerable computing resources.²⁴ We force all FHD foreground subtractions to model the GLEAM catalog as point sources, as PAPER-64 lacks the ability to properly resolve any of the extended sources in its field of view (FoV). An example of a single observation showing poorly resolved extended sources and the successful subtraction of Fornax A is shown in Figure 2, where Fornax A ($3^{\text{h}}22^{\text{m}}, -37^{\circ}12'$) is near the center of the FoV.

FHD’s Firstpass mode also includes a calibration of the data using the model visibilities and the method described in Salvini & Wijnholds (2014). However, the PAPER data analyzed here are already calibrated using the methods described in Ali et al. (2015). Hence, we allow FHD to fit a third-order polynomial to the time averaged per-frequency solutions for both phase and amplitude to correct for any gain scale or phase center discrepancies between the PAPER calibration and the GLEAM catalog. We calibrate and model 10,000 point sources of fixed flux density (>1 Jy) and position from the GLEAM catalog. Point sources are modeled in FHD as having a flat spectrum.

4.3. Excess High Delay Power in FHD Models

When modeling sources in FHD, each GLEAM point source is modeled as flat across frequency. In the absence of numerical errors, we would therefore expect that the only power that is pushed to higher delay modes in the delay transform is due to spectral leakage from a finite band and from the primary beam’s spectral structure. In principal, FHD can simulate precise and realistic spectral responses when computational resources are abundant; however, in this analysis approximations must be made. Numerical artifacts from these approximations in the visibility simulation process can introduce spurious spectral structure in the model visibilities. One particular source of artificial spectral structure in the algorithm used by FHD comes from its discrete sampling of the uv plane at a finite resolution. In this work, to balance the needs of precision and computational efficiency with a 128 day data set, we model the uv plane with a pixel size of 0.35λ on a side. This does not completely alleviate the numerical artifacts in the source spectrum; instead, in delay space, we find an aliasing floor beyond the horizon that is approximately three orders of magnitude smaller than the foreground amplitude, but still several orders of magnitude greater than a 21 cm EoR signal. When these model visibilities are subtracted from our PAPER visibilities, this high delay power is transferred into our residual

visibilities. With the sensitivity of this data set, this spurious spectral structure in the foreground model becomes the limiting factor in the analysis and sets a floor to any potential 21 cm signal limit.

To make progress, we low-pass filter our model visibilities using the iterative deconvolution filter with limits of $|\tau| \geq 90$ ns (for 30 m baselines). This removes a minimal amount of our model within the horizon limit while giving us the dynamic range to ensure that we are not adding power that would contaminate the EoR signal at high k -modes and near the horizon. We present a more in-depth analysis into this source of spurious spectral structure and the filtering we perform on model visibilities in Appendix B.

This filter indiscriminately removes high delay power from the model visibilities, including potential effects from the intrinsic spectral structure in the foregrounds or the instrument response. In this work, the foregrounds are modeled as a flat spectrum, and so possess no intrinsic high delay power; however, we do use the full frequency-dependent PAPER beam model in creating the model visibilities. Ultimately, we would like to include the full frequency-dependent model of the instrument and a frequency-dependent sky model in this kind of analysis. At present, however, the spurious structure limits our analysis and filtering is a necessary step to reach sensitivities relevant to it. We further discuss the implications of this analysis choice in Section 8.

5. Data and Preprocessing

5.1. PAPER

The drift-scan PAPER observations used for this analysis originate from the 2012 November–2013 March observing season of 128 days using the 64-element dual-polarization PAPER array. The data set is compressed in both time and frequency by averaging from 10.7 s time integrations to 42.9 s and from frequency channel widths of 97.7 kHz to 492.6 kHz using the delay/delay-rate filtering scheme described in Parsons et al. (2014). We identify and flag RFI at the 6σ level prior to calibration. Observations are then redundantly calibrated, also known as OMNICAL calibrated (Zheng et al. 2014), and absolute calibrated. Additional details of this data set can be found in Ali et al. (2015). Following these initial pre-processing steps we begin the foreground filtering and filtering+subtraction pipeline analysis as laid out in Figure 3. It should be noted that these visibilities undergo an additional calibration in FHD (step B), but after subtraction we return each visibility to their original OMNICAL calibration. In doing this, we should be mitigating any flux density scaling discrepancies or coordinate/pointing errors.

5.2. MWA

The MWA observations used are 2.6 hr from EoR0 ((R.A., decl.: $0^{\text{h}}, -27^{\circ}$) which is a region of the sky with minimal Galactic emissions (Beardsley et al. 2016)) where each visibility has a time integration of 2 s as opposed to the 42.9 s time-averaged integrations of PAPER. The MWA Phase I EoR observations (Jacobs et al. 2016; Pober et al. 2016; Trott et al. 2016) have an instantaneous bandwidth of 167–197 MHz across 384 channels. The narrow-band EoR redshift observations are taken over 95 channels (7.68 MHz) which correspond to a $\Delta z \approx 0.3$ for most measurements. The pipeline for comparing filtering versus filtering+subtraction for the MWA data is only

²⁴ For a single observation modeled with a uv -plane resolution of 0.35λ we used three cores from an Intel Xeon E5-2650 v4 with 80 GB of RAM with a runtime of ~ 20 min. Comparatively, for a resolution of 0.1λ using the same three cores and 100 GB results in a runtime of ~ 45 min.

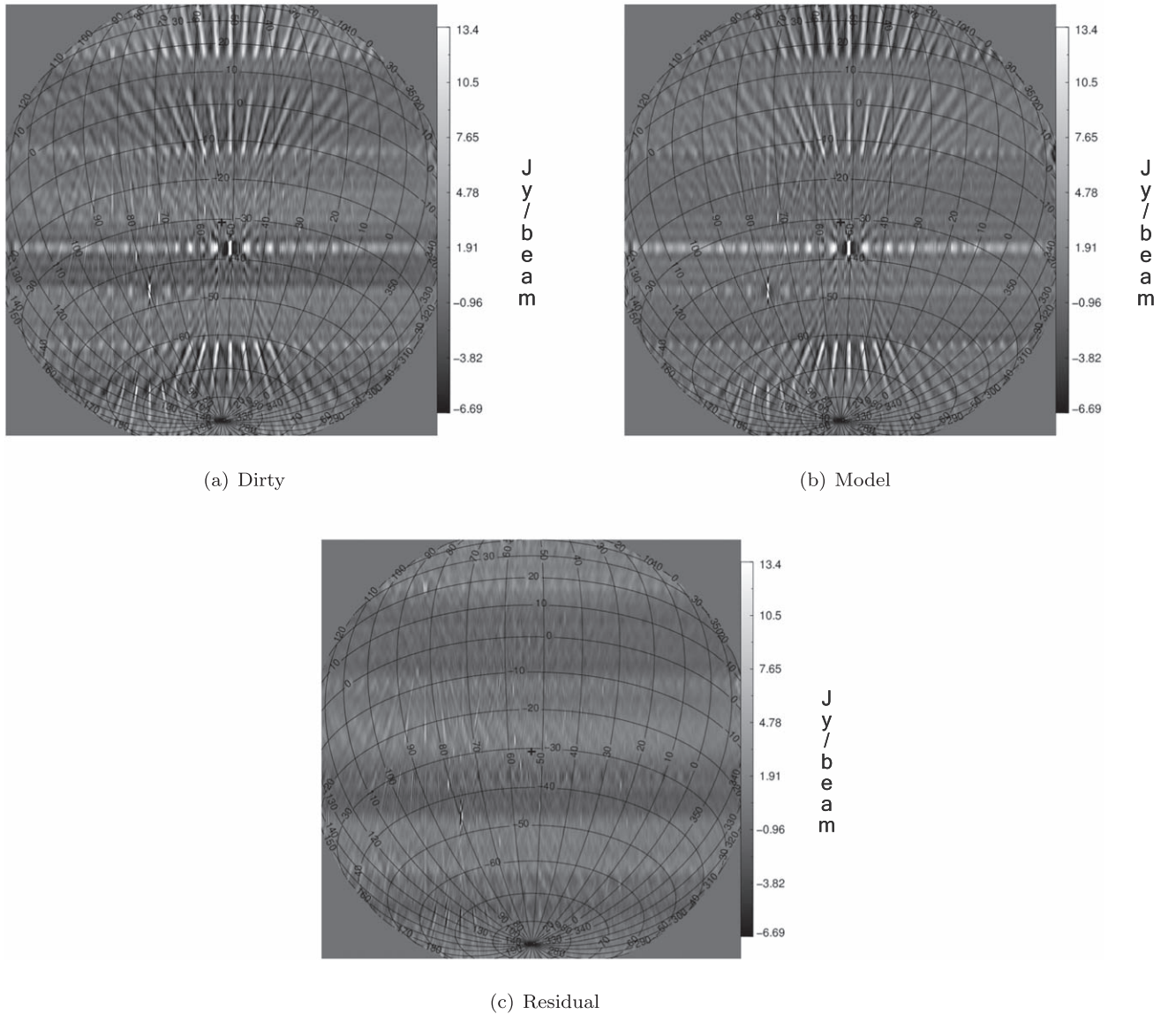


Figure 2. FHD-generated dirty (a), model (b), and residual (c) sky images of a single 10 min PAPER-64 observation. The two brightest sources in the FoV are Fornax A ($3^{\text{h}}22^{\text{m}}, -37^{\circ}12'$) and Pictor A ($5^{\text{h}}19^{\text{m}}, -45^{\circ}46'$). In the residual sky image, it can be seen that Fornax A is removed almost entirely, while Pictor A is subtracted but to a lesser degree. The partial subtraction of Pictor A is most likely due to a poor calibration and flux model in FHD, where the brightest sources (Fornax A) dominate the calibration process. Cygnus A can be seen toward the upper-left of the dirty and residual sky images, but is not present in the model because it is outside of the MWA GLEAM survey field.

similar to PAPER-64 up to step D and we omit the RFI flagging after the wide-band delay filter (step C).

6. Implementation on PAPER Data

The analysis focus for this work begins after the calibration steps described in Section 5. We emphasize only the critical steps required for the application of the combined foreground subtraction and filtering approach; a full description of the PAPER-64 analysis pipeline can be found in Ali et al. (2015). An abridged outline of the power spectrum pipeline can be seen in Figure 3, which shows the placement of the foreground subtraction step we add to the analysis. We choose to forgo the fringe rate filtering and the inverse covariance weighting at the end of the traditional PAPER-64 power spectrum pipeline. While these steps can improve the overall limit one can place on the 21 cm signal, they obscure many of the main effects seen

in our analysis and complicate interpretation of the results. However, it is possible to include inverse covariance weighting, fringe rate filtering, and signal loss in the filtering+subtraction power spectrum pipeline. These additional techniques can be included by following the results from a forthcoming paper (C. Cheng et al. 2018, in preparation) which discusses issues with applying inverse covariance weighting and the signal loss involved. To determine the effect of foreground subtraction on the analysis, we split our pipeline into the traditional PAPER-64 power spectrum pipeline, which we refer to as filtering, and one with FHD foreground subtraction included, referred to as filtering+subtraction. Figure 4 shows the effect each of these foreground removal steps has on the visibility amplitudes of 8.5 hr of data from a 30 m baseline. The first three steps (A, B, C) involve no averaging over days of observation; however, in panel D LST

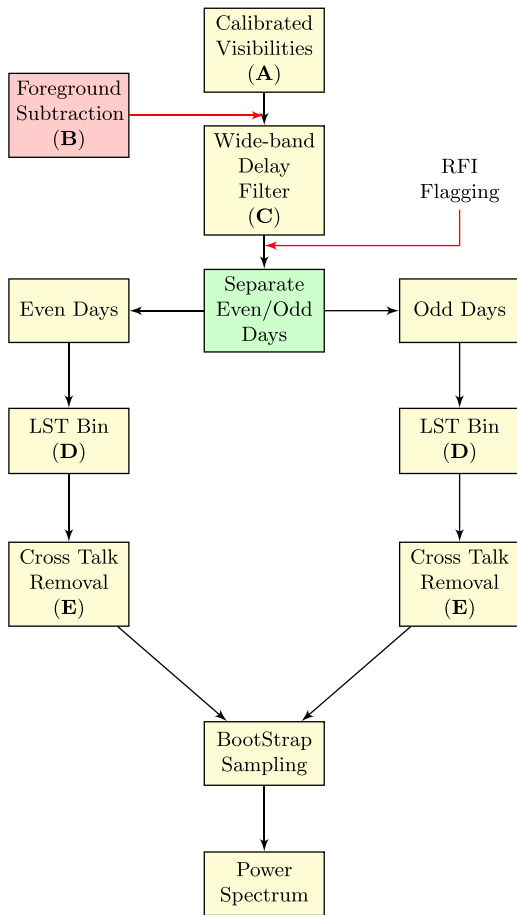


Figure 3. Abridged PAPER power spectrum pipeline used in processing visibilities for EoR measurements. After calibration (step A; described in Section 5), there is the option to subtract model foregrounds (step B). After the wide-band filtering (step C; described in Section 3), additional weak RFI is removed by flagging data with $>3\sigma$ deviation. Visibilities are split into even/odd days and averaged in local sidereal time (LST; step D). We cross multiply the even/odd LST binned visibilities to obtain an unbiased power spectrum estimator. Cross-talk removal (step E) is performed by using the full 8.5 hr of observations to ensure at least one full fringe period has elapsed. The PAPER power spectrum analysis from Ali et al. (2015) additionally uses a signal loss correction loop and inverse covariance weighting; these steps are not included here as they do not contribute to the understanding of filtering+subtraction. The letters labeling each step correspond to the steps in Figure 4.

binning is used to average over 64 days of observation (while the total data set is ~ 128 days, even and odd days are averaged separately). Note that omitting foreground subtraction (step B) results in plots C through E which are visually indistinguishable from the version shown. The white regions in Figure 4 are missing data due to flagging intermittent RFI which are recovered in step D due to LST binning. The RFI flagging that is consistent among all steps centered at 137 MHz with no recovery from LST binning is the ORBCOMM satellite system which is persistent across all observations and confined to around four frequency channels.

Depending upon the RFI strategy employed, frequency/time samples can be falsely identified as containing RFI, which is the case when flagging between steps C and D. The wide-band delay filtering decreases the narrow-band variance in the band center due to the Blackman–Harris window function; however, the wide-band variance remains comparatively large. This means that a reduction in the false-positive RFI identification rate can be achieved from either reducing the wide-band power

(foreground subtraction) or using a different window function in the filtering step prior to RFI flagging. We address the additional benefits of using a different window function in the filtering step and how it affects the power spectrum in Section 6.2.

In the final pre-processing step prior to the power spectrum estimate we apply cross-talk removal to all visibilities. We average per frequency over the entire 8.5 hr of visibilities which is then subtracted from each observation. By doing this we are able to account for the offset in the visibility complex plane due to cross-talk that becomes apparent after one full fringe period in our 30 m baselines.

For determining the statistical significance of the filtering +subtraction technique we empirically estimate errors on the PAPER-64 power spectra in Section 6.1 by bootstrapping. This is done in accordance with modifications suggested in C. Cheng et al. (2018, in preparation). We use 400 bootstrap samples taken from three redundant 30 m baseline types and over LST. To properly account for the error of differenced power spectra in Sections 6.1–6.3, we bootstrap over the distribution of differenced samples rather than use the combined error from each independent power spectrum. The differenced power spectra are created in parallel to make certain that the same random sample from LST and baseline are chosen.

6.1. Effect of Foreground Subtraction

We use the PAPER-64 power spectrum pipeline from Ali et al. (2015) as our point of comparison for determining how applying foreground subtraction prior to filtering can increase our sensitivity. The significance of the improved sensitivities is estimated by bootstrap sampling over our distribution of power spectra and differenced power spectra. While the foreground filter is performed across the entire 100 MHz PAPER band (hence the name “wide-band filter”), cosmological power spectra are restricted to a narrower range of frequencies to limit redshift evolution. In this analysis, we use 20 MHz of data for each cosmological power spectrum, but use a Blackman–Harris window function in this “narrow band” delay transform, giving an effective bandwidth of 10 MHz.

Power spectra from the band center at 150 MHz ($z = 8.4$) can be seen in Figure 5(a), where we compare each successive technique for foreground removal: no foreground mitigation (green), foreground subtraction (red), foreground filtering (blue), and filtering+subtraction (purple). The shaded gray region corresponds to modes inside the horizon, and the dashed black line corresponds to a delay of 15 ns beyond the horizon; the wide-band deconvolution is only allowed to fit modes with delays less than this value. We see that subtraction drops the foreground power by an order of magnitude within the horizon limit, with marginal improvements at higher delays. (Because of the Blackman–Harris window function in the narrow band delay transform, adjacent k -modes in the power spectrum are highly correlated, and so the improvements in the first mode beyond the horizon should be interpreted with caution.) The foreground filtering removes a very large fraction of power within the horizon limit, but also leads to significant improvements in the first several modes beyond the horizon. This behavior is indicative of reduced spectral leakage from modes within the horizon.

The power spectrum difference between filtering and filtering+subtraction can be seen in Figure 5(b), which shows a statistically significant ($\gtrsim 2\sigma$) improvement of modes within

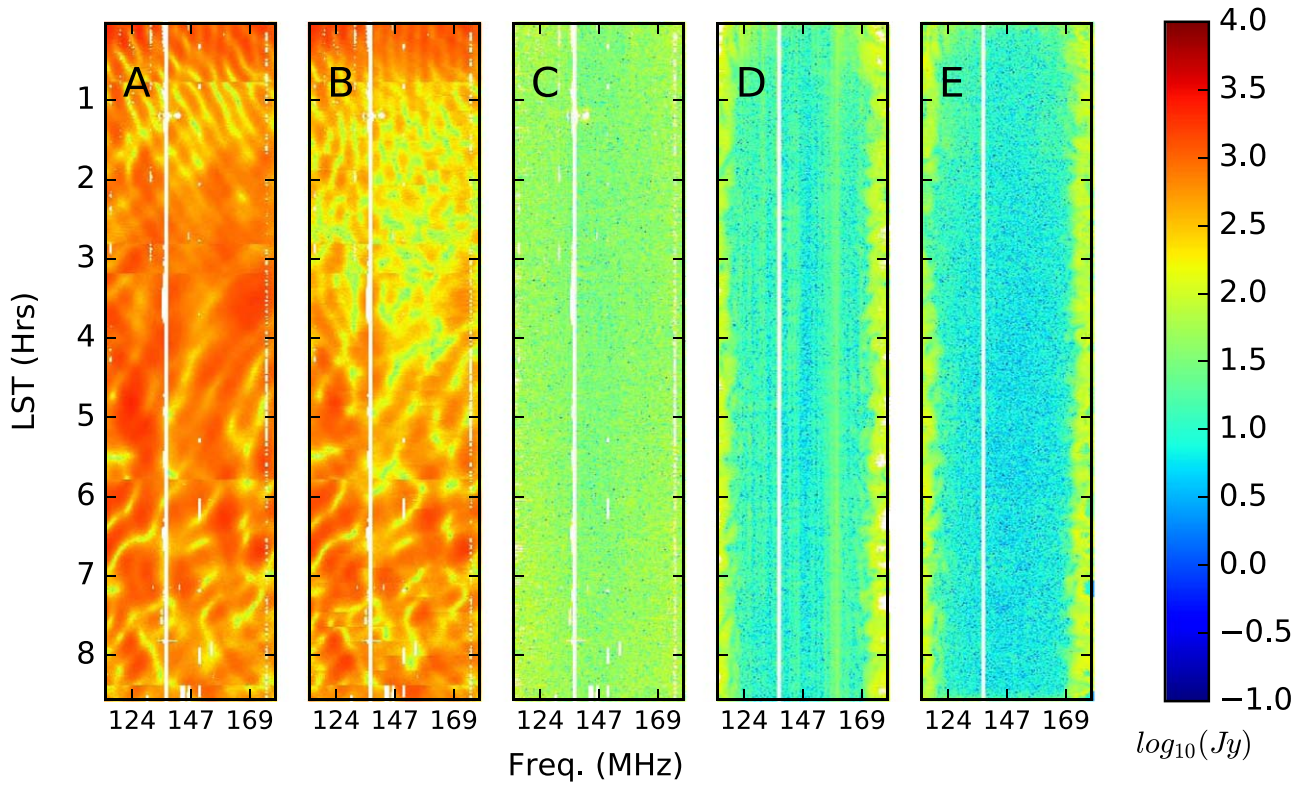


Figure 4. Sequential foreground removal steps of a fiducial 30 m PAPER-64 baseline. The steps are (A) OMNICAL calibrated baseline visibility, (B) foreground subtraction, (C) foreground filtering, (D) LST binning, and (E) cross-talk removal. Foreground subtraction can be seen to reduce power primarily due to Fornax A around 1–4 hr LST in (B), and additional foreground power is removed from smaller transiting sources up until the GLEAM catalog cutoff at 6^h30^m LST. The end result of applying the PAPER-64 power spectrum pipeline techniques results in approximately four orders of magnitude in amplitude of foreground suppression. A diagrammatic overview of how the pipeline progresses by step is shown in Figure 3. The discontinuities seen in LST in both A and B steps originate from gain variations due to applying the OMNICAL calibration on single 10 min observations.

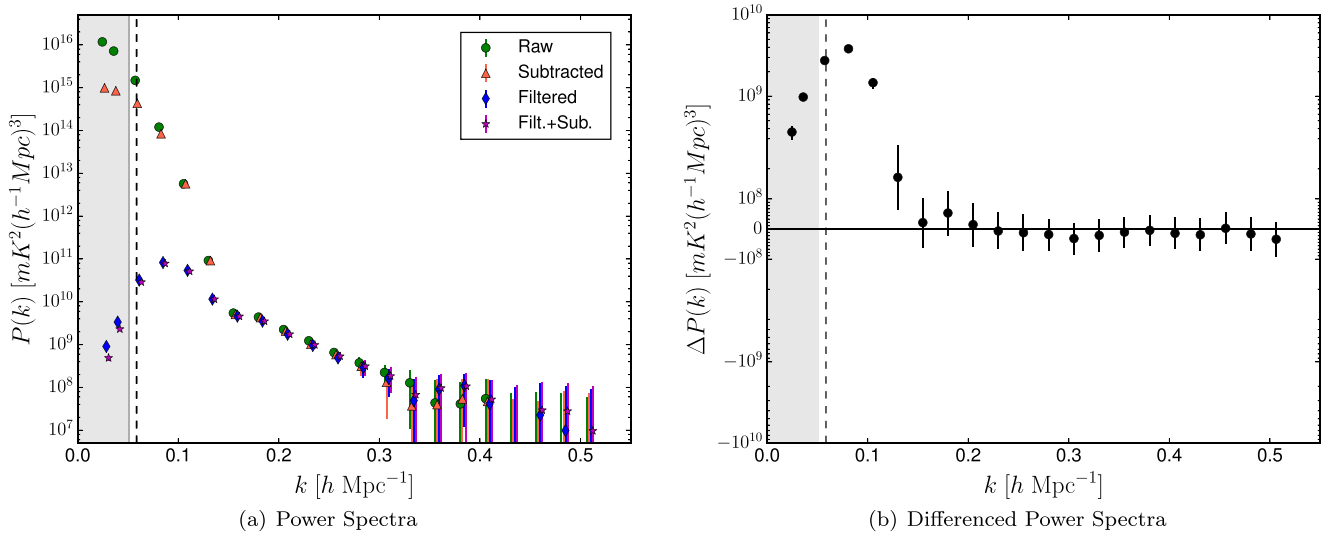


Figure 5. (a) Resulting power spectra from the 128 day LST binned PAPER-64 data set at band center ($z = 8.4$) focused on 1–6 hr LST, where the shaded region represents the horizon limit for a 30 m baseline and the broken vertical line is a 15 ns filtering extension. Power spectra correspond to each step of foreground removal: the raw PAPER-64 power spectrum (green), foreground subtracted (orange), foreground filtered (blue), and our filtered+subtracted technique (purple). (b) The differenced filtered and filtered+subtracted power spectra showing where we see improvements in sensitivity; more positive means greater sensitivity improvement due to reduction in spectral leakage. The first few modes nearest the horizon ($> k \approx 0.06$) show a statistically significant (2σ) improvement through the implementation of filtering and subtraction.

and near the horizon. At the most basic level, this result is expected. The model-based foreground subtraction has made the job of the wide-band delay filter easier: there is less power it

needs to remove. In particular, when foregrounds are subtracted from the raw visibilities, we reduce the amount of power that rings off of sharp discontinuities in the frequency-sampling

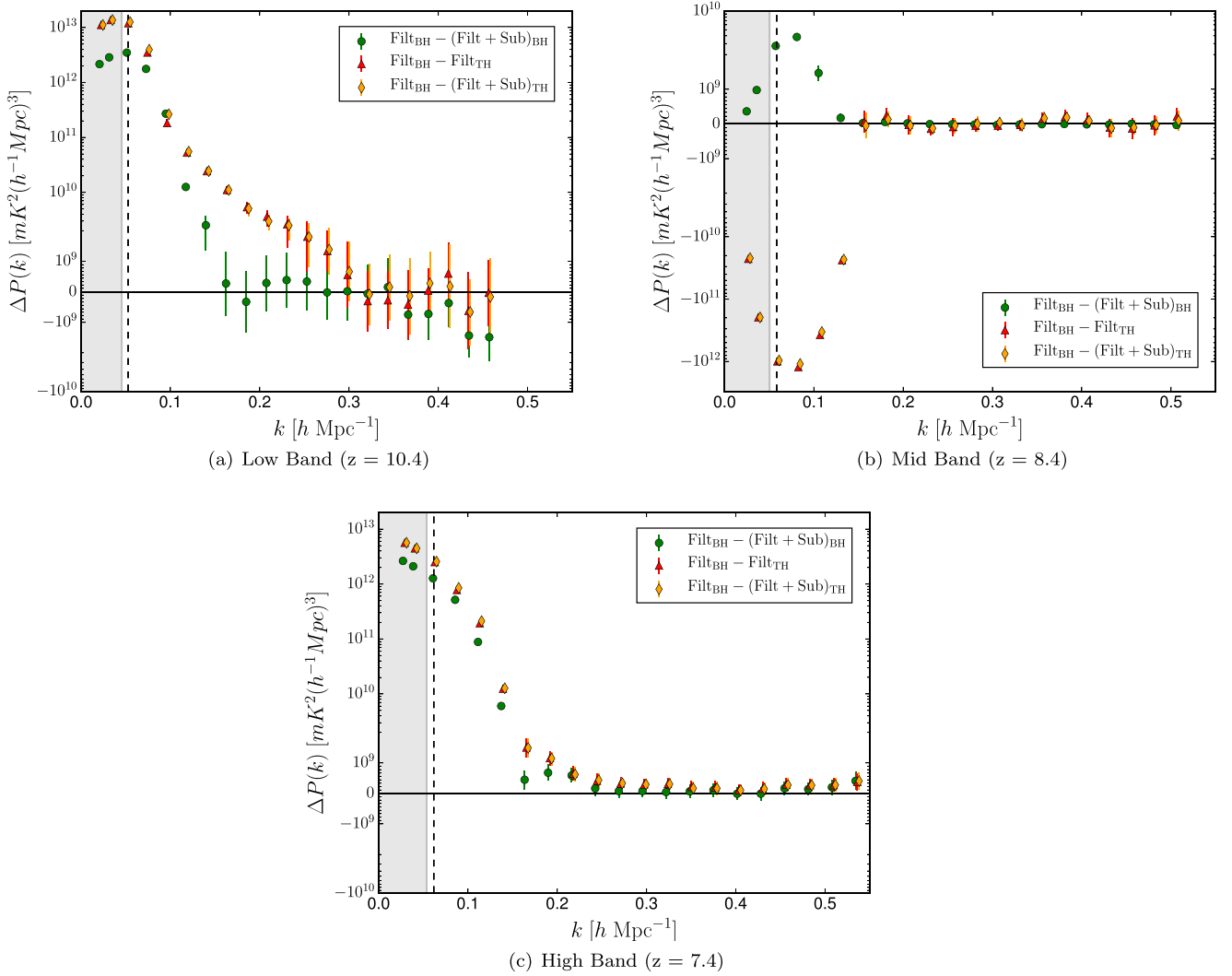


Figure 6. Power spectrum difference between filtering and filtering+subtraction at different band locations comparing the effectiveness of window function choice on power removed during the wide-band filtering step, where again more positive shows an improvement by both filtering and subtracting foregrounds. We compare the standard Blackman–Harris (BH) to the top-hat (TH) window function. We should expect that the TH window function gives us the maximum amount of foreground removal at band edges because of the equal weighting across the entire band. A symmetric improvement about band center is shown in (a) and (c) where the switch from BH to TH window function increases the reduction in spectral leakage in the low (high) band by $\sim 145\%$ (113%) and with subtraction $\sim 169\%$ (125%) at $k \approx 0.11 \text{ hMpc}^{-1}$. The band center plot (b) demonstrates that the BH window function is the ideal choice regardless of filtering or filtering+subtraction when compared to the TH window.

function when taking the delay transform. In the PAPER data set, the ORBCOMM satellite band centered at 137.5 MHz spans several channels and is always flagged. This creates a very sharp discontinuity that leads to strong ringing of foreground power throughout visibility space. Because the frequency-sampling function is known, the iterative wide-band filter can, in principle, remove this scattered power itself. But, the deconvolution algorithm is not perfect, and it appears that reducing the total amount of foreground power available to scatter in a delay transform leads to better performance of the wide-band deconvolution filter. Put another way, the wide-band foreground filter has an effectively fixed dynamic range that it can achieve between the brightest foreground contaminated modes and the limits in the EoR window. Even though the model visibilities contain no intrinsic power in the EoR window, reducing the power in the brightest foreground contaminated modes improves the end result because we are limited by the dynamic range of the wide-band filter.

6.2. Performance Near Band Edges

One of the strengths of the PAPER experiment is its wide instantaneous bandwidth which covers 100 to 200 MHz ($z \sim 6\text{--}13$). The data analyzed in Section 6.1 were centered around 150 MHz, where past analyses have shown the wide-band foreground filter (using a Blackman–Harris window function) to be most effective (Jacobs et al. 2015). In this section, we demonstrate the effectiveness of filtering+subtraction nearer to the edges of PAPER’s frequency band with power spectra at 124 and 169 MHz (corresponding to $z = 10.4$ and 7.4, respectively).

The green points in Figure 6 show the difference in power spectra made using filtering and filtering+subtraction at all three redshifts: $z = 10.4$ (a), 8.4 (b), and 7.4 (c). (Note that the green points in Figure 6(b) are the same data shown in Figure 5(b).) These data show that filtering+subtraction removes significantly more power from the first few modes outside the horizon than filtering alone. Compared with the $z = 8.4$ results in Figure 5(a),

we see that filtering+subtraction removes one to two more orders of magnitude of foreground power than it does at the band center. This increased effectiveness of our technique at the band edges comes more from foreground subtraction itself than any interplay between the subtraction and the filtering, which drove the improvements at band center. This effect is primarily because the Blackman–Harris window in the wide-band filtering step specifically down-weights the band edges. Therefore, we expect the wide-band filter to perform comparatively poorly at the band edges, as was seen in Jacobs et al. (2015). Subtraction should, however, significantly help at the band edges since it is able to remove power here that the wide-band filter cannot. Alternatively, we might expect that a different choice of window function in the filtering step should give dramatic improvements at high/low redshifts when compared to the standard pipeline.²⁵

The PAPER power spectrum pipeline uses the Blackman–Harris window function when applying the iterative deconvolution filter, which gives the result of maximum foreground avoidance at band center. This choice of window function, however, produces limited improvements at the band edges due to down-weighting prior to delay transforming. Typically, if one were to forgo the use of a window function (i.e., using a top-hat window) in the filtering of data with discontinuities, this would result in significant spectral leakage, but this is not the case here. We can overcome spectral leakage in this instance because we are deconvolving both the window and sampling function from our filtered visibility. There are, however, limitations in doing this because deconvolution is a computationally demanding task. Furthermore, the product of the window and sampling functions can be complicated, and varies from visibility to visibility, so in some cases the iterative nature of this filtering may fail to converge. We therefore might expect the top-hat window function to be an improvement over the Blackman–Harris near the band edges because it equally weights every frequency channel (as long as convergence in the iteration is reached). The points in Figure 6 are a difference of power spectra demonstrating the effect of window function choice in the wide-band filter (more positive is better). For these points, the foreground filtering+subtraction analysis was applied in two cases (green; orange) to show the effect without a top-hat window function used in the wide-band transform and after using this window. We also show the change from Blackman–Harris to top-hat (red) in a filtering-only case to provide a point of reference for the inclusion of the foreground subtraction in the filtering+subtraction. We see that the top-hat filter leads to significant improvements at the band edges—almost an order of magnitude larger near the horizon than the improvements we see from filtering+subtraction with a Blackman–Harris window. At the band center ($z = 8.4$), however, we see that the top-hat filter gives a significantly worse result near the horizon: below k of $\sim 1.5 h \text{ Mpc}^{-1}$, it leaves significantly more residual foreground emission, making the difference negative. We expect that the Blackman–Harris should outperform the top-hat window function in this case, since the latter has more difficult sidelobes to deconvolve.

Lastly, the orange points in Figure 6 show the difference between filtering with a Blackman–Harris window and filtering+subtraction with a top-hat window. In all three bands, we see that filtering+subtraction with a top-hat leads to even more of an improvement than filtering with a top-hat alone (red). At the band

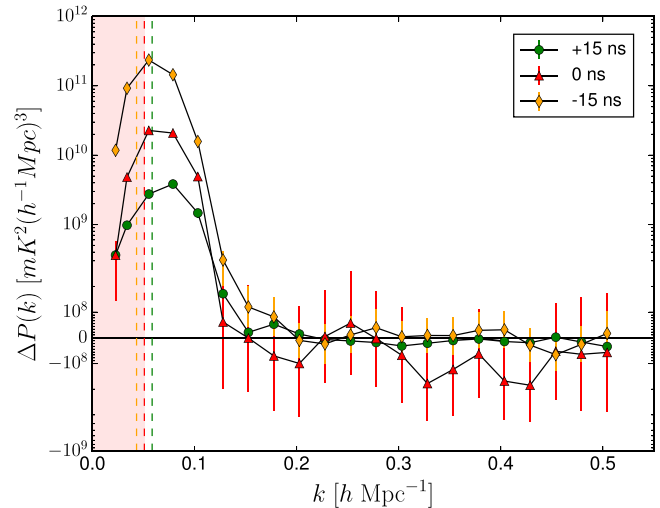


Figure 7. Power spectra differences (filtering minus filtering+subtraction) for different sizes of filter: 15 ns beyond the horizon limit (green), at the horizon (red), and 15 ns inside the horizon (orange). Smaller filters leave more of k space available for EoR measurements (modes within the filter have effectively 100% signal loss), and subtraction is seen to result in bigger improvements when smaller filter sizes are used. With improved sky models, subtraction can therefore play an important role in maximizing the recovery of the 21 cm signal.

edges, the majority of the improvement over filtering with a Blackman–Harris appears to come from the switch to the top-hat window, but the best results come when first subtracting a foreground model and then applying the wide-band deconvolution filter using a top-hat window. At the band center, the Blackman–Harris proves the best choice of window function in the wide-band filtering step.

6.3. Improved Measurements within the Horizon

Delay filtering of foregrounds has been shown to be a powerful technique for 21 cm data analysis, but it does have significant limitations. Modes within and directly outside the horizon (due to the 15 ns extension) have effectively 100% EoR signal loss when filtering and therefore become useless for cosmological measurements (see Appendix A). This is of course unfortunate, as the EoR signal is brightest at these large scales. To begin to recover some of these modes, we can potentially use foreground subtraction prior to filtering and then reduce the filter’s extent in k back toward or even inside of the horizon. This means that we can maximize the effect of subtraction mitigating the foreground contamination by purposefully reducing the performance of filtering at the cost of sensitivity at higher k -modes. Figure 7 shows power spectrum differences between filtering and filtering+subtraction for three choices of filter width: at the horizon (0 ns, red), 15 ns beyond the horizon, as used in the analysis above (green), and 15 ns inside of the horizon (orange). We see that the improvements coming from the subtraction step grow larger the less aggressive the filter, i.e., filtering+subtraction results in the biggest improvement when the filter is set to 15 ns inside the horizon (–15 ns). Overall, the total residual foreground power in k -modes near the horizon is minimized with the most aggressive filter (+15 ns), but as we continue to improve foreground models and the efficacy of subtraction, it will be worthwhile to revisit this analysis and see whether k -modes at or near the horizon can be turned into useful limits even in a foreground filtering approach.

²⁵ Alternatively, Liu et al. (2014b) describe a method for quantifying the leakage between k -bins from choice of window function therefore reducing emphasis on which window function is used; we do not explore this effect here.

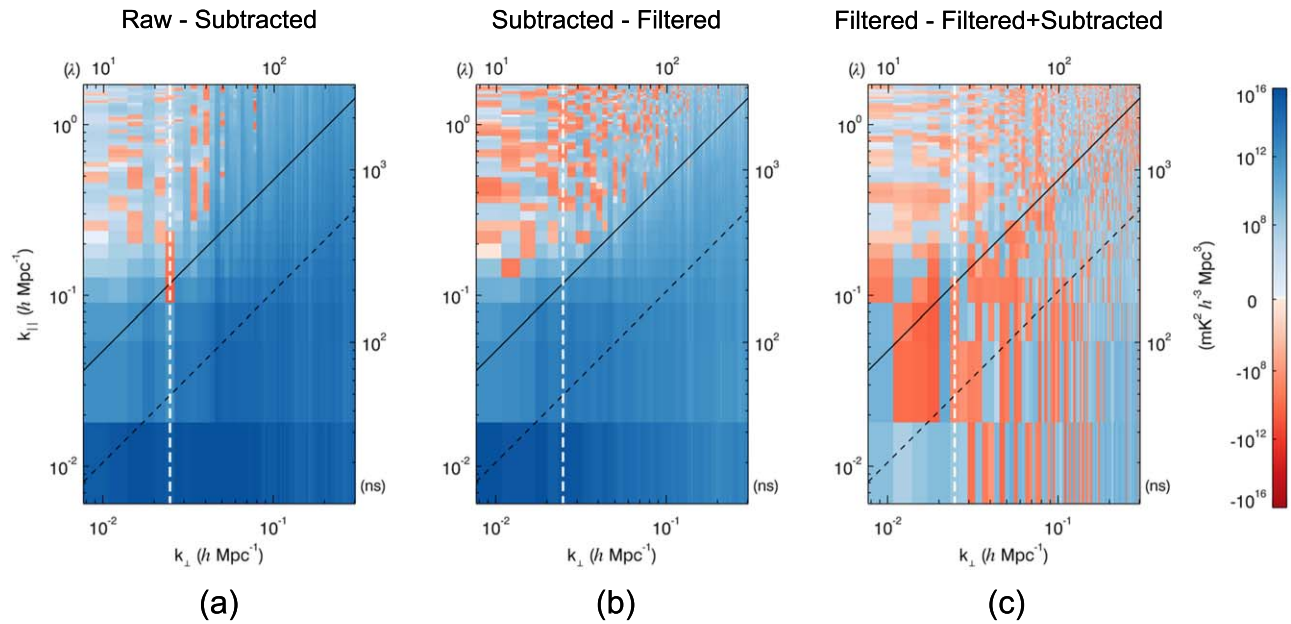


Figure 8. MWA 2D wedge power spectra difference plots showing the comparison between each foreground removal step where blue (red) indicates an improvement (worsening) between steps. The solid diagonal line represents the horizon limit while the broken line represents the FWHM of the MWA primary beam (Sutinjo et al. 2015). The vertical white broken line marks a 30 m baseline, equivalent in length to that used in the PAPER-64 analysis. The difference between the raw power spectrum with no foreground removal and one with FHD foreground subtraction is shown in (a) which gives an expected improvement inside of and beyond the horizon limit. The comparison between FHD foreground subtraction and wide-band filtering (b), shows an additional clear improvement over the standard MWA subtraction pipeline at the majority of k_{\perp} -modes nearest the horizon. Finally, comparing the use of filtering with both filtering+subtraction in panel (c), we do not see any clear improvement, but comparison with the PAPER-64 results suggests that we have reached a noise limit where any improvements are well below the sensitivity available with only 3 hr of data.

7. Hybrid Foreground Removal Technique Applied to MWA Phase I

To demonstrate the robustness and general applicability of the hybrid foreground removal technique across multiple instruments, we apply it to the 3 hr of MWA Phase I observations as described in Section 5.2. In many ways, these observations represent the extreme opposite of PAPER-64. The MWA Phase I has 128 tiles²⁶ laid out in a minimum redundancy configuration, giving it a much fuller (u, v) coverage than PAPER-64. It also has baselines up to nearly 3 km in length, giving it a resolution of order a few arcminutes, a factor of ~ 10 improvement over PAPER-64. FHD was also designed specifically for use with MWA interferometry data and the GLEAM catalog used for subtraction is a direct MWA product. We should thus expect better relative foreground subtraction when compared to PAPER-64.

The results of applying the hybrid technique on approximately 3 hr of MWA Phase I observations at band center (182.415 MHz) are shown in Figure 8 in “xx” instrument polarization. For the most accessible comparison to PAPER-64 hybrid foreground removal we continue to use the difference between power spectra but in the form of the cylindrically averaged 2D differenced power spectra. This gives us the ability to approximately compare similar MWA and PAPER 30 m baseline difference power spectra and to view the effect of foreground filtering+subtraction across multiple MWA baseline types. In these difference plots, blue indicates a region where the first step of the analysis has more power, and red indicates a region where the second step has more power. In Figure 8(a) we show the difference between raw data (calibrated, but no foreground subtraction) and the standard foreground

subtraction used in the MWA power spectrum pipeline (as performed in e.g., Barry et al. 2016; Jacobs et al. 2016, and Pober et al. 2016). We see, unsurprisingly, that foreground subtraction removes a significant amount of power inside the wedge, but there are also improvements well beyond the horizon limit (shown as a solid diagonal line). These improvements are on the same order of magnitude ($10^{16} \text{ mK}^2 (h^{-1} \text{ Mpc})^3$) within the horizon) as seen in Figure 5(a) between the raw (green) and subtracted (red). Figure 8(b) compares foreground subtraction with the wide-band deconvolution foreground filtering. Filtering removes more power within the horizon than subtraction, but we also see an improvement immediately outside of the horizon limit across all k_{\perp} . Note that no “buffer” was used outside the horizon in the foreground filtering, so any power removed outside the horizon is almost certainly due to reduced spectral leakage. At low k_{\perp} and high k_{\parallel} we approach a noise floor; since only 3 hr of data were used, it is considerably higher than the noise floor in the PAPER-64 analysis. In Figure 8(c), comparing the filtered and filtered+subtracted power spectra, we see a similar noise level, but throughout all of k space. If we assume our results for the MWA should closely mirror those from PAPER-64, then improvements at band center due to filtering+subtraction should be on the order of $\sim 10^9 \text{ mK}^2 (h^{-1} \text{ Mpc})^3$ which is below the noise level we see here.

We also see similar results to the PAPER-64 analysis when looking at the MWA band edges (high/low redshift). Based on the PAPER-64 analysis, we would expect improvements of $\sim 10^{12} - 10^{13} \text{ mK}^2 (h^{-1} \text{ Mpc})^3$ from using filtering+subtraction over just filtering. This is consistent with the results shown in Figure 9, which has a uniform decrease in power within the horizon and a slight, though noisy, improvement in the window. While we have shown a top-hat to be a much improved wide-band window for analysis near the band edges, MWA visibilities have a 2 s time

²⁶ MWA tiles consist of 16 individual dipole antenna elements that are steered with an analog beamformer, as opposed to the single dipole element used for drift scanning in PAPER-64.

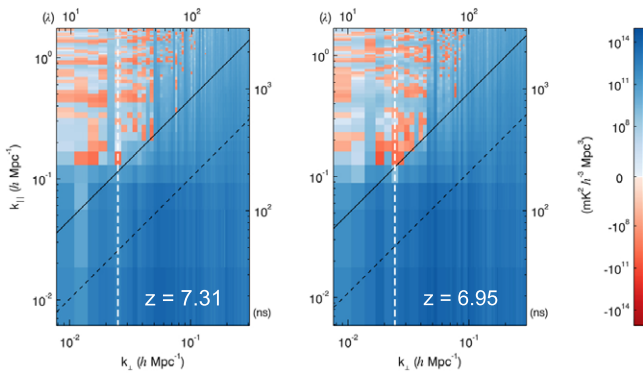


Figure 9. MWA 2D power spectra difference plots between filtering and filtering+subtraction at low band (7.31) and high band (6.95). The results are generally similar to the equivalent PAPER-64 difference power spectra at the band edges. Improvements near the horizon are due to subtraction compensating for the down-weighting of band edges when windowing.

resolution, compared to 10 s with PAPER. This lower signal-to-noise ratio (S/N) coupled with a top-hat window can make it more difficult for the iterative deconvolution filter to converge. Using a wide-band Blackman–Harris window function, even when analyzing data near the band edges, is therefore important to help convergence in this instance.

8. Conclusions

The next generation of radio interferometers attempting to make a statistical detection of the 21 cm EoR power spectrum will require the removal of as much foreground power as possible. To date, even the most promising foreground removal techniques leave behind residual contamination which is well above the most optimistically bright EoR signals. In this work, we have presented a hybrid technique which combines both model-based foreground subtraction and delay-based foreground filtering. In doing so, we have demonstrated the following.

1. Even in parts of the EoR window, residuals from foreground filtering exist which are brighter than an EoR signal.
2. Foreground subtraction can be successfully applied to arrays with sparse (u, v) coverage (e.g., PAPER-64) using source catalogs derived from other arrays with high (u, v) coverage (e.g., the MWA). The limiting factor in our ability to perform this subtraction is the numerical fidelity with which we can forward model visibilities for the large (1088 hr) PAPER data set.
3. Combining filtering and subtraction results in statistically significant improvements across the entire band, with the greatest improvements at band edges.
4. The choice of window function is an important ingredient in wide-band iterative deconvolution foreground filtering, especially when analyzing data at frequencies away from the band center.
5. Foreground subtraction can potentially enable less aggressive foreground filtering (i.e., removal of fewer modes near/inside the horizon), allowing for EoR measurements within the horizon.
6. Despite a more complicated frequency response (including the coarse band harmonics) and beam shape, foreground filtering can be successfully applied to

MWA visibilities and results in a significant improvement over subtraction alone.

7. Improvements with filtering+subtraction are more readily seen as S/N improves, therefore we should expect for any improvements to sensitivity to become more visible with longer integration times.

The EoR signal is brightest at low k -modes, so foreground removal nearest (or inside) the horizon limit can have the greatest impact on overall sensitivity (Pofer et al. 2016). We have seen that subtraction with a reduction in the net power prior to filtering can reduce leakage into the modes right outside the horizon. It would therefore be reasonable to subtract as much foreground power as possible—both diffuse and point sources—prior to filtering for the most minimally contaminated EoR power spectrum estimates across all redshifts. We demonstrate this hybrid foreground subtraction and filtering technique as a proof of concept, and with additional computational resources to increase the uv -plane resolution to below the 0.35λ used here, we expect that this technique could be drastically improved upon. This would alleviate the need to low-pass filter our model visibilities and should result in near-horizon improvements by both modeling the spectral response of the instrument and reducing the overall dynamic range that the iterative deconvolution filter needs to overcome.

Furthermore, with an improved sky and instrument model we should expect subtraction to provide a more consistent improvement across all visibilities and not just those containing our brightest foreground sources (Fornax A and Pictor A). More specifically, as weak and smaller sources are included in the analysis we approach a “subtraction floor” due to position errors between PAPER observations and the GLEAM catalog. This leads to improper or partial subtractions that result in no net removal of foreground power. Therefore improvements resulting from these changes in the case of PAPER-64, would stem directly from improved catalog positions and flux measurements, and the introduction of a diffuse model, but not necessarily from the additional modeling and subtraction of more weaker (<1 Jy) point sources.

Implementing the iterative deconvolution wide-band filter can be a computationally expensive process, especially when compounded with foreground subtraction, which itself is laborious. The filtering step can also be accomplished without the use of the iterative deconvolution filter by carrying out a more traditional filtering in the delay domain. A sparse sampling function with missing data will, however, give significant ringing in the visibility. Ringing occurs when a signal is band-limited, which is approximately the case for a raw visibility where the foregrounds are $>10^5$ when compared to anything beyond the horizon. This ringing is substantially reduced when subtraction is applied prior, potentially bringing the residual foregrounds to a point where they are no longer within the approximate band-limited regime. If subtraction can remove enough power to enable the use of an FIR foreground filter, the computational load and pipeline processing time can be significantly reduced.

Future work will rely on applying this hybrid foreground removal approach to the newest season of observations from the Hydrogen Epoch of Reionization Array (HERA). Hardware improvements for HERA-37 alone should increase the sensitivity by a factor of ~ 5 over PAPER-128 (DeBoer et al. 2017). HERA’s beam in terms of complexity positions it between PAPER and MWA, while having better horizon

suppression than either of them (Thyagarajan et al. 2015). This places additional importance on mitigating residual foreground contamination and puts us in a new regime for testing the hybrid foreground removal limitations as sensitivities increase. The inclusion of this hybrid approach to our most sensitive 21 cm EoR interferometer should lead to the tightest, least contaminated power spectrum constraints over the redshift range of $7 < z < 11$.

This material is based upon work supported by the National Aeronautics and Space Administration under the NASA Rhode Island Space Grant Consortium. J.R.K., J.C.P., and A.R.P. would like to acknowledge the support from NSF Grants No. #1440343 and No. #1636646. This material is additionally based upon work supported by the NSF under Grant No. #1506024. A.P.B. is supported by an NSF Astronomy and Astrophysics Post-doctoral Fellowship under award #1701440. A.L. acknowledges support for this work by NASA through Hubble Fellowship grant #HST-HF2-51363.001-A awarded by the Space Telescope Science Institute, which is operated by the Association of Universities for Research in Astronomy, Inc., for NASA, under contract NAS5-26555. This scientific work makes use of the Murchison Radio-astronomy Observatory, operated by CSIRO. We acknowledge the Wajarri Yamatji people as the traditional owners of the Observatory site. Support for the operation of the MWA is provided by the Australian Government (NCRIS), under a contract to Curtin University administered by Astronomy Australia Limited. We acknowledge the Pawsey Supercomputing Centre which is supported by the Western Australian and Australian Governments. Additionally, this research was conducted using computational resources and services at the Center for Computation and Visualization, Brown University.

Appendix A

Wide-band Deconvolution Filter Signal Loss

The iterative wide-band deconvolution filter has the unfortunate side effect of destroying information at k -modes within our “EoR window” nearest the horizon limit. The original analysis done in Ali et al. (2015) approached signal loss using a Blackman–Harris window function and a residual threshold (ratio of final to initial delay-space component) of 10^{-9} . We extend the original analysis by quantifying the signal loss at all k -modes accessible by the PAPER-64 instrument for both the Blackman–Harris and top-hat windows using several values of the residual tolerance. This is by no means an exhaustive analysis, but covers the range of filters used in this paper and other similar analyses from the PAPER collaboration. The amount of signal recovered is identified by injecting a known “EoR-like” signal (V_{eor}) to a simulated PAPER-64 baseline visibility containing foregrounds (V_{fgs}). The visibility including the injected EoR signal $V_{\text{fgs+eor}}$ and V_{fgs} are then wide-band filtered. We then create the power spectra P_{fgs} and $P_{\text{fgs+eor}}$ and we compare the recovered signal in the form of

$$\bar{Y}(k)_{\text{Frac. of Signal Rec.}} = \left\langle \frac{\text{Filtered}(P_{\text{eor+data}}) - \text{Filtered}(P_{\text{data}})}{P_{\text{eor}}} \right\rangle. \quad (5)$$

where $\langle \cdot \rangle$ represents the ensemble average and $\bar{Y}(k)_{\text{Frac. of Signal Rec.}}$ is the ensemble average over the fraction of signal that is recovered from the wide-band filtering process. We can get an idea of the typical (average) or extreme limit (3σ) for signal loss by looking at the ensemble average of recovered signal to injected signal over

$N = 1000$ trials where we vary both injected signal realization and power ($10^{-10} \cdot P_{\text{data}} \leq P_{\text{eor}} \leq 10^{-4} \cdot P_{\text{data}}$). The fraction of signal recovered when using a Blackman–Harris window and top-hat window is shown in Figures 10(a) and (b). The top-hat window outperforms the Blackman–Harris with respect to recovering signal in the mode nearest the horizon filter limit ($k \approx 0.079 h \text{ Mpc}^{-1}$) because we sacrifice dynamic range for reducing correlation between adjacent k -modes. While both signal loss analyses in Figures 10(a) and (b) demonstrate fairly similar worst-case ($\bar{Y} + 3\sigma$) signal loss across the tolerances demonstrated, its important to note that the magnitude of foregrounds removed from within the filter limit and the number of iterations to convergence (time) varies between tolerance. This leaves us with the optimal choice of 10^{-9} for our iterative wide-band deconvolution filter.

We also investigate how the increasing width of the filter with increasing baseline length affects signal loss. The results of applying the same signal loss analysis but now to baselines of lengths 30 m, 120 m, and 300 m are shown in Figure 10(c). We see that moving the filter limit gives us very similar results as the standard 30 m filter limit, simply pushed further in k : modes inside the horizon limit have very large values of signal loss, while modes outside the horizon are essentially unaffected. This analysis is useful in understanding the MWA 2D power spectra, which contain different length baselines, seen in Figures 8 and 9.

Appendix B

Creating Model Visibilities with Fast Holographic Deconvolution

In this work, we use FHD (Sullivan et al. 2012) to create model visibilities from a foreground source catalog and instrument model. These model visibilities are then directly subtracted from the visibility data to perform our foreground subtraction step. The FHD software package can perform many different operations, including calibration, image-based deconvolution, and visibility simulation; the use of FHD as a visibility simulator has been presented in Barry et al. (2016) and Pober et al. (2016). Here, we describe the key steps in FHD visibility simulation to understand where the numerical artifacts described in Section 4.3 appear.

When using a point source catalog as input, FHD uses a discrete Fourier transform to take a source at a floating point location in (R.A., decl.) to a discretized uv plane. Both the size of pixels in this uv plane and the number of pixels (i.e., the maximum extent of the uv plane) are free parameters in FHD. All uv planes for each point source being simulated are summed to create a model uv sky-brightness distribution. Model visibilities for each baseline are then created by integrating the product of the uv response function (the Fourier transform of the primary beam from image domain to uv space; Morales & Matejek 2009) at the (u, v) coordinate of the baseline of interest and the model uv sky-brightness distribution. Because the uv plane has been discretized into pixels, however, this integral is approximated as a discrete sum and can introduce numerical errors, particularly as a function of frequency (since the (u, v) coordinates of a baseline are frequency dependent).

To illustrate these errors, we show the delay spectrum of an FHD-generated model visibility for a 30 m east–west baseline and a single source in Figure 11. Different colored curves correspond to different pixel areas in the uv plane in units of wavelength: 0.1 λ (orange), 0.2 λ (blue), and 0.35 λ (red). Increasing the uv -plane resolution clearly mitigates the high delay power created by spurious spectral structure, but comes

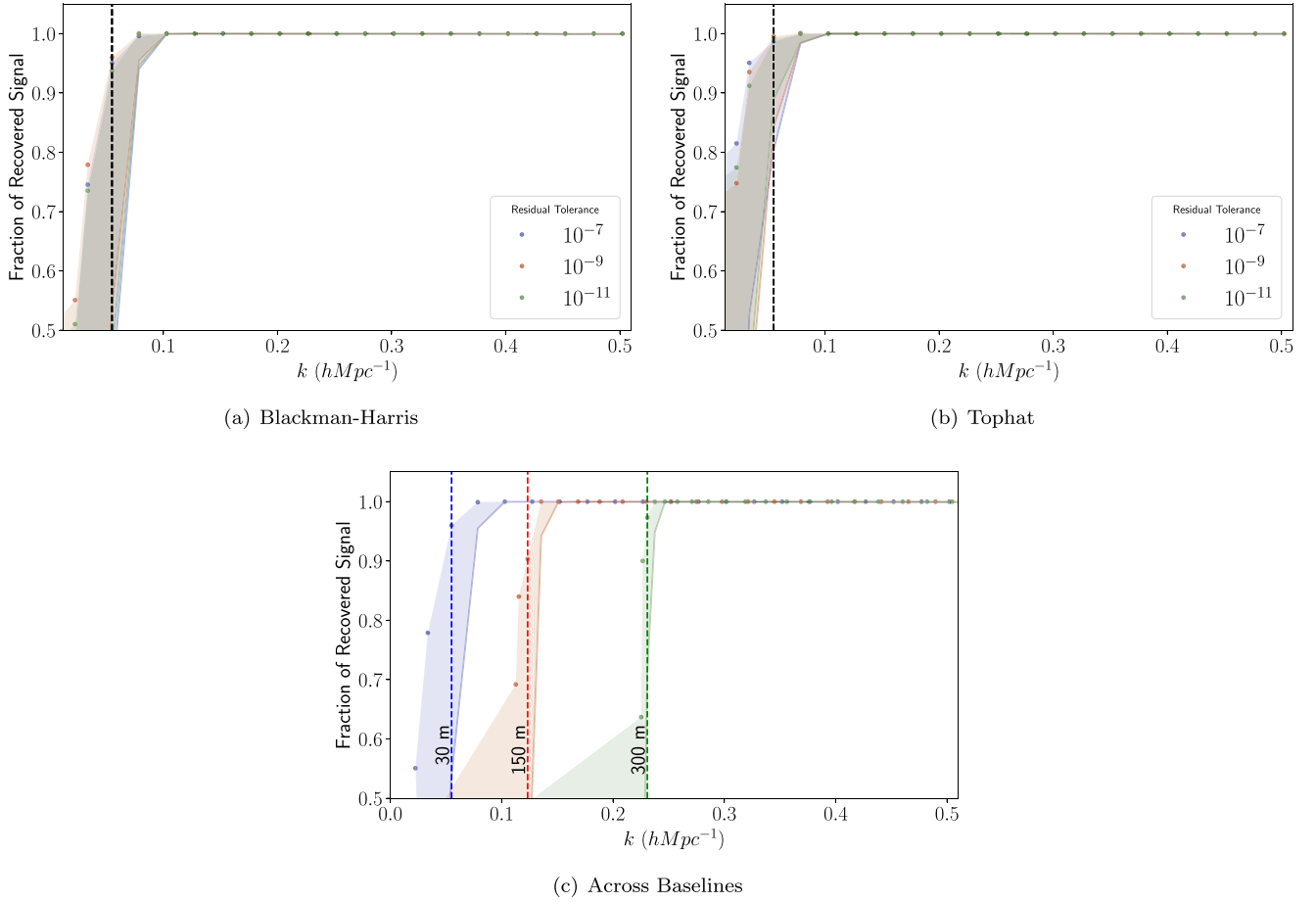


Figure 10. (a) Narrow-band power spectrum signal recovered after performing the wide-band iterative deconvolution filter using a Blackman–Harris window function. The dots represent the average signal recovered at each k -mode and the shaded region is the 3σ limit for our worst-case signal recovery. Using the filtering residual tolerance of 10^{-9} we see that for the k -mode right outside the filter limit at $k = 0.079 h Mpc^{-1}$ we can expect an average signal loss of $8.2 \times 10^{-2}\%$ with a 3σ upper-limit of 4.6%. (b) As (a); however, we replace the Blackman–Harris window with a top-hat window. The typical signal loss of the mode nearest the filter limit at $k = 0.079 h Mpc^{-1}$ is $8.4 \times 10^{-2}\%$ with a 3σ upper-limit of 1.6%. (c) Although the PAPER-64 analysis consists of only one baseline type (30 m) we also want to demonstrate the fraction of signal recovered over different length baselines (wider horizon filter limits) which is important to our MWA foreground subtraction and filtering analysis. The residual tolerance is 10^{-9} with a Blackman–Harris window applied, and the filtering is performed over baselines of the length 30, 120, and 300 m. We show that the amount of signal recovered should essentially be a translation in k when compared to (a) and (b).

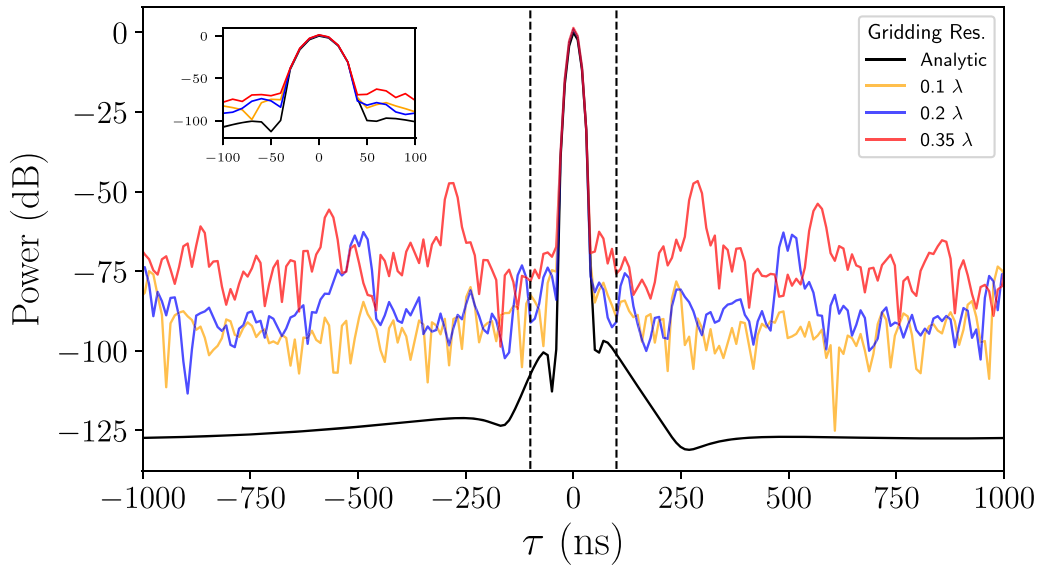


Figure 11. Simulation of a single point source in a 30 m baseline visibility at zenith for different uv -plane resolutions in FHD: 0.1λ (orange), 0.2λ (blue), and 0.35λ (red). We also show the analytic response we expect for the same source (black). The inset shows the normalized peak spectra relative to the analytic source. At smaller uv -gridding resolutions, we see the power at high delays decreases while the peak source brightness converges to the analytic source. These model delay spectra examples also demonstrate a clear aliasing floor and thus lead to our motivation for filtering out high delays prior to subtraction.

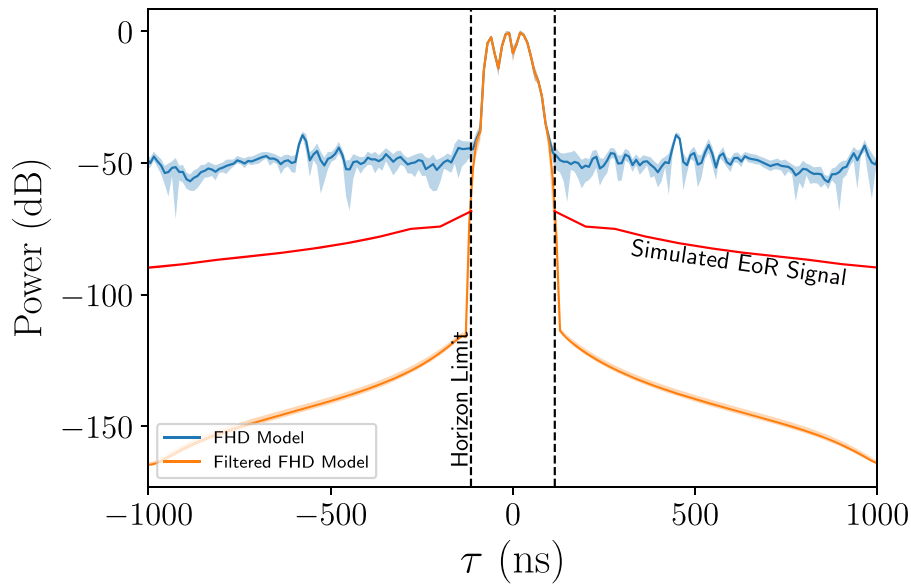


Figure 12. Many sources example (compare to Figure 11) of a delay transformed and peak-power-normalized FHD model visibility ($k_{\text{res}} = .35\lambda$) for a 30 m baseline averaged over a single observation (blue), and the same model after low-pass filtering (orange) both with shaded regions demonstrating the variance over time. A Blackman–Harris window function has been applied in both cases. In the unaltered curve, large-amplitude spectral structure can be seen outside of the delay horizon, >115 ns. As described in the text, the origin of this high delay power is not physical. A fiducial 21 cm power spectrum at 50% reionization (Lidz et al. 2008) (red) is shown as a reference to demonstrate that the FHD model must be filtered prior to subtraction so that our EoR signal is not contaminated.

at the cost of increased computational resources and would not be feasible without specialized high RAM machines. The black curve represents the analytic value assuming a Blackman–Harris window was used in the Fourier transform to delay space. The gridding resolution 0.35λ is the resolution used in this analysis, and was used strictly for the purpose of efficiently calibrating, modeling, and subtracting our large data set; running the full analysis at these higher resolutions is not computationally feasible, and even then, it does not bring the numerical error significantly below the level of the EoR signal (which is also approximately 80 dB below the foregrounds). Small flux density scaling errors between the different resolutions are a point of concern, but are largely mitigated in our analysis, as we effectively calibrate the flux scale of the FHD model to the absolutely calibrated PAPER data.

As noted in Section 4.3, this high delay power is the limiting factor in our analysis. If it is not removed, it sets a floor to best obtainable limits on the EoR signal with PAPER-64 data. To remedy this problem we use our iterative deconvolution filter to low-pass filter the 0.35λ model visibilities with filter horizon of 90 ns for our 30 m baselines. Figure 12 illustrates the effect of this filter. The delay spectrum of the FHD model prior to filtering is shown in blue and the delay spectrum after filtering is shown in orange. For comparison, a model EoR signal is shown in red. We acknowledge that this filter will also remove any *real* high delay power (introduced by the instrument)²⁷ from the model visibilities. Because the high delay power in the model is a limiting systematic, however, we choose to forgo the possibility of using the model to subtract high delay power from the data. The fact that we still see improvements in the power spectrum (Section 6.1) shows that we are reducing the overall power within the horizon to the point where our filtering process is not dynamic range limited. Going forward, using either a modified version of FHD or another (likely more computationally intensive) code for simulating visibilities, we

would not have to low-pass filter our models and the improvement of the filtering+subtraction technique near the horizon should come from both effects: removing the chromatic footprint of the PAPER antenna response and reducing the dynamic range requirements on the delay filter.

ORCID iDs

Joshua R. Kerrigan <https://orcid.org/0000-0002-1876-272X>
 Jonathan C. Pober <https://orcid.org/0000-0002-3492-0433>
 Adam P. Beardsley <https://orcid.org/0000-0001-9428-8233>
 James E. Aguirre <https://orcid.org/0000-0002-4810-666X>
 Gianni Bernardi <https://orcid.org/0000-0002-0916-7443>
 Chris L. Carilli <https://orcid.org/0000-0001-6647-3861>
 David R. DeBoer <https://orcid.org/0000-0003-3197-2294>
 Joshua S. Dillon <https://orcid.org/0000-0003-3336-9958>
 Daniel C. Jacobs <https://orcid.org/0000-0002-0917-2269>
 Saul A. Kohn <https://orcid.org/0000-0001-6744-5328>
 Adrian Liu <https://orcid.org/0000-0001-6876-0928>

References

- Ali, Z. S., Parsons, A. R., Zheng, H., et al. 2015, *ApJ*, 809, 61
 Barry, N., Hazelton, B., Sullivan, I., Morales, M. F., & Pober, J. C. 2016, *MNRAS*, 461, 3135
 Beardsley, A. P., Hazelton, B. J., Sullivan, I. S., et al. 2016, *ApJ*, 833, 102
 Chapman, E., Abdalla, F. B., Bobin, J., et al. 2013, *MNRAS*, 429, 165
 Cohen, A. S., Lane, W. M., Cotton, W. D., et al. 2007, *AJ*, 134, 1245
 DeBoer, D. R., Parsons, A. R., Aguirre, J. E., et al. 2017, *PASP*, 129, 045001
 Dillon, J. S., Liu, A., & Tegmark, M. 2013, *PhRvD*, 87, 043005
 Dillon, J. S., Neben, A. R., Hewitt, J. N., et al. 2015, *PhRvD*, 91, 123011
 Ewall-Wice, A., Dillon, J. S., Hewitt, J. N., et al. 2016, *MNRAS*, 460, 4320
 Högbom, J. A. 1974, *A&AS*, 15, 417
 Hurley-Walker, N., Callingham, J. R., Hancock, P. J., et al. 2017, *MNRAS*, 464, 1146
 Jacobs, D. C., Hazelton, B. J., Trott, C. M., et al. 2016, *ApJ*, 825, 114
 Jacobs, D. C., Parsons, A. R., Aguirre, J. E., et al. 2013, *ApJ*, 776, 108
 Jacobs, D. C., Pober, J. C., Parsons, A. R., et al. 2015, *ApJ*, 801, 51
 Lane, W. M., Cotton, W. D., van Velzen, S., et al. 2014, *yCat*, 8097

²⁷ Because we model the sources on the sky as a flat spectrum, they will not be a source of high delay power.

- Lidz, A., Zahn, O., McQuinn, M., Zaldarriaga, M., & Hernquist, L. 2008, *ApJ*, 680, 962
- Liu, A., Parsons, A. R., & Trott, C. M. 2014a, *PhRvD*, 90, 023018
- Liu, A., Parsons, A. R., & Trott, C. M. 2014b, *PhRvD*, 90, 023019
- Liu, A., & Tegmark, M. 2011, *PhRvD*, 83, 103006
- Morales, M. F., Hazelton, B., Sullivan, I., & Beardsley, A. 2012, *ApJ*, 752, 137
- Morales, M. F., & Matejek, M. 2009, *MNRAS*, 400, 1814
- Offringa, A. R., Trott, C. M., Hurley-Walker, N., et al. 2016, *MNRAS*, 458, 1057
- Paciga, G., Albert, J. G., Bandura, K., et al. 2013, *MNRAS*, 433, 639
- Parsons, A. R., & Backer, D. C. 2009, *AJ*, 138, 219
- Parsons, A. R., Backer, D. C., Foster, G. S., et al. 2010, *AJ*, 139, 1468
- Parsons, A. R., Liu, A., Aguirre, J. E., et al. 2014, *ApJ*, 788, 106
- Parsons, A. R., Pober, J. C., Aguirre, J. E., et al. 2012, *ApJ*, 756, 165
- Patil, A. H., Yatawatta, S., Koopmans, L. V. E., et al. 2017, *ApJ*, 838, 65
- Pober, J. C., Hazelton, B. J., Beardsley, A. P., et al. 2016, *ApJ*, 819, 8
- Pober, J. C., Parsons, A. R., Aguirre, J. E., et al. 2013, *ApJL*, 768, L36
- Pober, J. C., Parsons, A. R., Jacobs, D. C., et al. 2012, *AJ*, 143, 53
- Salvini, S., & Wijnholds, S. J. 2014, *A&A*, 571, A97
- Sullivan, I. S., Morales, M. F., Hazelton, B. J., et al. 2012, *ApJ*, 759, 17
- Sutinjo, A. T., Colegate, T. M., Wayth, R. B., et al. 2015, *ITAP*, 63, 5433
- Thyagarajan, N., Jacobs, D. C., Bowman, J. D., et al. 2015, *ApJ*, 804, 14
- Thyagarajan, N., Parsons, A. R., DeBoer, D. R., et al. 2016, *ApJ*, 825, 9
- Tingay, S. J., Goeke, R., Bowman, J. D., et al. 2013, *PASA*, 30, e007
- Trott, C. M., Pindor, B., Procopio, P., et al. 2016, *ApJ*, 818, 139
- van Haarlem, M. P., Wise, M. W., Gunst, A. W., et al. 2013, *A&A*, 556, A2
- Vedantham, H., Udaya Shankar, N., & Subrahmanyan, R. 2012a, *ApJ*, 745, 176
- Vedantham, H., Udaya Shankar, N., & Subrahmanyan, R. 2012b, *ApJ*, 745, 176
- Wang, J., Xu, H., An, T., et al. 2013, *ApJ*, 763, 90
- Zheng, H., Tegmark, M., Buza, V., et al. 2014, *MNRAS*, 445, 1084